ACS APPLIED MATERIALS & INTERFACES

Research Article

www.acsami.org

Improved Open-Circuit Voltage in Polymer/Oxide-Nanoarray Hybrid Solar Cells by Formation of Homogeneous Metal Oxide Core/Shell Structures

Fan Wu, Qi Cui, Zeliang Qiu, Changwen Liu, Hui Zhang, Wei Shen, and Mingtai Wang*

Institute of Plasma Physics and Key Lab of Novel Thin Film Solar Cells, Chinese Academy of Sciences, Hefei 230031, P. R. China

Supporting Information

ABSTRACT: Incorporation of vertically aligned nanorod/nanowire arrays of metal oxide (oxide-NAs) with a polymer can produce efficient hybrid solar cells with an ideal bulk-heterojunction architecture. However, polymer/oxide-NAs solar cells still suffer from a rather low (normally, < 0.4 V) open-circuit voltage (V_{oc}). Here we demonstrate, for the first time, a novel strategy to improve the V_{oc} in polymer/oxide-NAs solar cells by formation of homogeneous core/shell structures and reveal the intrinsic principles involved therein. A feasible hydrothermal−solvothermal combined method is developed for preparing homogeneous core/shell nanoarrays of metal oxides with a single-crystalline nanorod as core and the aggregation layer of corresponding metal oxide quantum dots (QDs) as shell, and the shell thickness (L) is easily controlled by the solvothermal reaction time for growing QDs on the nanorod. The core/shell formation dramatically improves the device V_{oc} up to ca. 0.7−0.8 V depending on L. Based on steady-state and dynamic measurements, as well as modeling by space-charge-limited current method, it is found that the improved V_{oc} originates from the up-shifted conduction band edge in the core by the interfacial dipole field resulting from the decreased mobility difference between photogenerated electrons and holes after the shell growth, which increases the energy difference between the quasi-Fermi levels of photogenerated electrons in the core and holes in the polymer for a higher V_{oc}. Our results indicate that increasing V_{oc} by the core/shell strategy seems not to be dependent on the kinds of metal oxides.

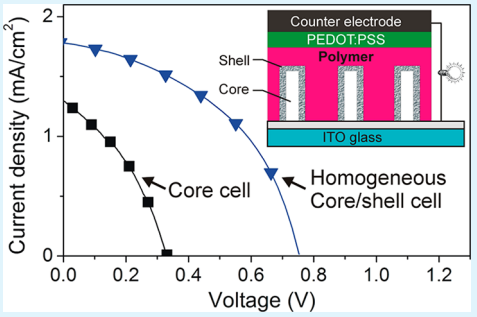

KEYWORDS: *solar cells, interface, nanoarray, metal oxide, electron mobility*

1. INTRODUCTION

Hybrid polymer-based solar cells (HPSCs) that use conjugated polymers as electron donor (D) and inorganic semiconductor nanocrystals as electron acceptor (A) in a bulk-heterojunction (BHJ) architecture have shown promise for future photovoltaic devices.[1−3] Using nanoarrays (NAs) of vertically aligned nanorod/nanowire to replace the disordered A-phase pathways formed by nanoparticles can provide an ideal BHJ architecture for efficient solar cells. The metal oxide nanoarrays (oxide-NAs) (e.g., ZnO-NAs and TiO_2-NAs) are often used to fabricate such aligned BHJ devices, because of their nontoxicity, high electron mobility and thermal stability.[4−6] However, the power conversion efficiency (η) in polymer/ZnO-NA[1,7−9] or polymer/TiO_2-NA[10,11] solar cells is not high yet (normally, η < 0.6%), even though η = 3.9% has been achieved by incorporating PCBM into the HPSCs based on ZnO-NAs and poly(3-hexylthiophene) (P3HT);[12] in particular, the open-circuit voltage (V_{oc}) in the polymer/oxide-NA devices is generally rather low (0.1−0.5 V), which significantly limits the device η. To establish the methods for achieving high V_{oc} and understand the principles therein are the challenges in access to efficient polymer/oxide-NA solar cells.

Modification at the D/A interface with organic molecules generally enhances the short-circuit current (J_{sc}) in polymer/oxide-NAs devices by increasing the interfacial compatibility, but hardly improves V_{oc}.[8,10,13−15] Coating inorganic layers (e.g., TiO_2,[16] TiO_x,[17] CdS,[18] CdSe,[19,20] PbS[21]) on oxide-NAs to form heterogeneous structures has been demonstrated to increase significantly the V_{oc} in polymer/Oxide-NA solar cells. Deposition of crystalline TiO_2 or amorphous titanium oxide (TiO_x) on ZnO-NA provided ZnO/$TiO_{2(x)}$-core/shell nanorod arrays (ZnO-TiO_2-NAs[16] or ZnO-TiO_x-NAs[17]), where the P3HT/ZnO-TiO_2-NA solar cells had a V_{oc} up to 0.55 V and an increased J_{sc} depending on the TiO_2 shell thickness, whereas the P3HT/ZnO-TiO_x-NA devices exhibited a much higher V_{oc} (~0.80 V) than P3HT/ZnO-NA devices but a much lower J_{sc} due to the barrier effect of TiO_x layer on the charge transfer from the polymer to ZnO;[17] sensitization of ZnO-NAs with CdS (or PbS) quantum dots (QDs) produced the V_{oc} up to 0.85 V (or 0.59 V) in their HPSCs, along with an increased J_{sc} to a certain extent.[18,21] Heterogeneous modification inevitably generates the interfacial defects due to lattice mismatch[22] or lattice expansion[23] to affect the charge transport and recombination. Moreover, the effects of the heterogeneous

Received: January 22, 2013
Accepted: March 21, 2013
Published: April 9, 2013

shell layers on device performance are hitherto not clearly understood yet. For examples, the improved V_{oc} by the TiO_x shell formation is explained from the decrease in reverse saturation current based on a modified ideal diode equation;[17] the CdS-sensitization effect on V_{oc} is attributed to the band offset between CdS and ZnO in the cascading energy band structure formed upon CdS deposition.[18] However, it is hard to correlate the loads of the modifiers (e.g., CdS-QDs) with the device performance in those explanations.

The factors determining V_{oc} in HPSCs are still the subject of much debate. Normally, the energy difference between the highest occupied molecular orbital (HOMO) level of the donor and the conduction band edge of the acceptor determines the maximum V_{oc}.[1,24,25] Recent studies demonstrated that the change of V_{oc} in HPSCs may correlate with the altered band alignment at the D/A interface due to the presence of interfacial dipoles.[9,26−28] For example, the improved V_{oc} in the P3HT/ZnO-NA device subjected to the UV/ozone treatment of ZnO surface is believed to originate from the band alignment changed by interfacial dipole formation between P3HT and ZnO;[9] the molecular dipoles have been used as modifier to shift the band positions of TiO_2[26] or ZnO[27,28] for adjusting V_{oc} in their HPSC devices. In addition, Blom and co-workers[29,30] found that the balance between the carrier extraction and the energy loss via charge recombination led to a distinct optimization in the carrier mobility for efficient fullerene-based devices, and too high mobility for charge extraction will lead to a low device V_{oc}, but the process governing V_{oc} was not fully understood even though a correlation between a low V_{oc} and a reduced difference between the quasi-Fermi levels of electrons and holes was observed. There is still insufficient knowledge concerning the intrinsic correlation between V_{oc} and charge carrier mobility in HPSCs, whereas a few studies had been reported on the relationship between carrier mobility and J_{sc}.[29,31]

In this paper, we develop a novel and feasible strategy to improve the V_{oc} in polymer/oxide-NAs solar cells by formation of homogeneous core/shell nanoarrays. As depicted in Figure 1,

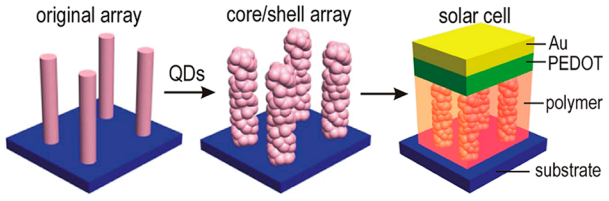

Figure 1. Illustration for formation of homogeneous metal oxide core/shell nanoarrays and their solar cell architecture.

the hydrothermally preformed oxide-NAs are modified by their corresponding QDs through a solvothermal process, generating core/shell nanoarrays (referred to as oxide-NR-QD-NAs); then the core/shell nanoarrays are infiltrated with poly(2-methoxy-5-(2-ethylhexyloxy)-1,4-phenylene vinylene) (MEH-PPV) to fabricate solar cells. Results show that the high V_{oc} subjected to the core/shell formation originates from the generation of interfacial dipoles due to the decreased mobility difference between photogenerated electrons and holes.

2. EXPERIMENTAL SECTION

Synthesis of ZnO-NR-QD-NAs. ZnO-NA was hydrothermally grown by suspending the ZnO-coated indium tin oxide (ITO) conducting glass (<15 Ω/□, Shenzhen Laibao Hi-Tech Co., Ltd., China) upside down in an aqueous solution of zinc nitrate hexahydrate (0.025 M) (Sinopharm Chemical Reagent Co., Ltd.) and hexamethylenetetramine (0.025 M) (99.99%, Alfa Aesar) at 90 °C as reported previously.[32] The ZnO-NA was put upside down in a Teflon-lined stainless steel autoclave (100 mL volume), and added 60 mL zinc acetate solution in ethanol (0.02 M); the sealed autoclave was heated at 95 °C for a defined time (t = 4, 4.5, or 6 h) for the solvothermal growth of ZnO-QDs, to get ZnO-NR-QD-NA with a specific shell thickness; finally, after the autoclave naturally cooled to room temperature, the ZnO-NR-QD-NA was taken out, thoroughly rinsed with alcohol and dried in a N_2 flow.

Synthesis of TiO_2-NR-QD-NAs. Fluoride-doped tin oxide (FTO) coated glass sheet (14 Ω/□, 400 nm FTO in thickness, Nippon Sheet Glass Co.) was first patterned into stripes (12 × 4 mm^2) on the glass substrate by HCl solution and Zn powder, and washed twice with acetone, isopropanol, and deionized water, respectively, in which the ultrasonic treatment for 10 min was done for each wash. TiO_2-NA was hydrothermally grown on FTO surface.[33] After a thermal annealing in air at 450 °C for 30 min, the TiO_2-NA substrate was put upside down in a Teflon-lined stainless steel autoclave (100 mL volume), and added 60 mL titanium isopropoxide solution in ethanol (0.1 M); the sealed autoclave was heated at 200 °C for 4 h for the solvothermal growth of TiO_2-QDs, to get TiO_2-NR-QD-NA. After the autoclave naturally cooled to room temperature, the substrate was taken out, thoroughly rinsed with alcohol and dried in a N_2 flow.

Device Fabrication. MEH-PPV (average M_n = 40000−70000, Aldrich) and poly(3,4-ethylene dioxythiophene):poly(styrenesulfonate) (PEDOT:PSS) (Clevios P HC V4, H. C. Starck) was commercially obtained. Solar cells were fabricated by the procedure similar to our previous reports,[13,32,34] where the polymer layer was deposited on the top of nanoarray by spin-coating (1500 rpm, 40 s) the MEH-PPV solution in chlorobenzene (5 mg/mL) under ambient conditions for twice, followed by annealing at 150 °C under N_2 atmosphere for 10 min to ensure the polymer infiltration into the interspaces between nanorods. After the spin-coating of PEDOT:PSS (2000 rpm, 60 s), the sample was heated for 15 min at 100 °C under a nitrogen atmosphere. Finally, a gold electrode (100 nm) was evaporated through a shadow mask to form an overlapped area between ITO and Au of 3 mm × 3 mm, which defined as the effective device area. The electron-only devices were fabricated the procedure same to the solar cell assembly except for the PEDOT/Au top electrode was replaced with the evaporated LiF (1 nm)/Al (100 nm).

Characterization. X-ray diffraction (XRD) patterns were recorded on an MXP18AHF X-ray diffractometer with Cu K_α irradiation (λ = 1.54056 Å). Scanning electron microscopy (SEM) measurements were carried out on a field-emission scanning electron microscopy (FE-SEM, FEI Sirion200). Transmission electron microscopy (TEM) and high-resolution TEM (HRTEM) studies were performed on a JEOL-2010 microscope under an acceleration voltage of 200 kV. Photoluminescence (PL) measurements were performed on a Hitachi F-7000 spectrofluorophotometer. Solar cells were characterized with current−voltage (J−V) measurements and intensity modulated photovoltage spectroscopy (IMVS). Steady-state J−V curves were measured under AM1.5 illumination (100 mW/cm^2, calibrated with a standard crystalline silicon solar cell) under ambient conditions on a 94023A Oriel Sol3A solar simulator (Newport Stratford, Inc.) with a 450 W xenon lamp as the light source, and the J−V data were collected with an Oriel I−V test station (PVIV-1A, Keithley 2400 Source Meter, Labview 2009 SP1 GUI Software, Newport). IMVS measurements were done on a controlled intensity modulated photo spectroscopy (CIMPS) (Zahner Co., Germany) in ambient conditions, as described previously.[32,34] The J−V curves of the solar cells and the electron-only devices in the dark were collected on the CIMPS system with ITO contact as negative electrode.

3. RESULTS AND DISCUSSION

3.1. Formation of Core/Shell ZnO Nanoarrays. SEM image (Figure 2a) shows that the initial ZnO-NA is vertically aligned on ITO substrate, with a length of ∼400 nm, a diameter

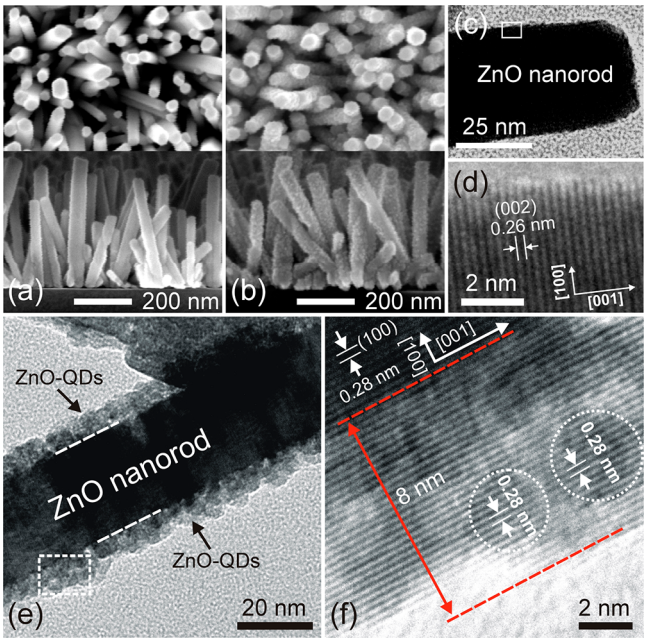

Figure 2. SEM images of ZnO-NA (a) before and (b) after deposition of ZnO-QDs. (c, e) TEM and (d, f) HRTEM images of (c, d) ZnO nanorod and (e, f) ZnO-NR-QD nanorod with L = 8 nm, in which the ZnO and ZnO-NR-QD nanorods were obtained from the samples in a and b, respectively. The HRTEM images were taken from the marked regions on the corresponding TEM images, and the cycles in (f) identify individual ZnO-QDs.

of 20−50 nm and a number density of about 4−5 × $10^2/\mu m^2$, agreeing with previous results;[32,35] after deposition of ZnO-QDs, the morphology of ZnO-NA is not remarkably altered, but ZnO nanorod surfaces become decorated by small particles (Figure 2b). The ZnO-NA was indexed to wurtzite ZnO and the single-crystalline ZnO nanorods therein grew along [001] crystallographic direction,[35,36] as indicated by XRD pattern (see Figure S1 in the Supporting Information). TEM image (Figure 2c) shows that the surface of original ZnO nanorod is quite smooth, and HRTEM image (Figure 2d) confirms the ZnO nanorod growth along [001] direction. After the ZnO-QDs growth, the ZnO nanorod surface is coated with a shell layer (Figure 2e), and the XRD pattern of the core/shell sample (see Figure S1 in the Supporting Information) was only indexed to wurtzite ZnO. As shown in Figure 2f, both core and shell exhibit the same oriented lattice fringes without lattice mismatch or distortion, where the marked interplanar spacings of 0.28 nm correspond to the (100) lattice plane of wurtzite ZnO, suggesting that the shell consisting of ZnO-QDs with a size of 2−4 nm was actually epitaxially grown on ZnO nanorod surface. The aggregation of epitaxially grown ZnO-QDs on ZnO nanorods is similar to the growth of ZnO nanoparticles on ZnS nanobelt.[37] Both TEM and XRD results clearly demonstrate that, with the preformed ZnO-NA as a template, the ZnO-NR-QD-NA core/shell nanoarray with a single-crystalline ZnO nanorod serves as core and an aggregation layer of ZnO-QDs as shell has been successfully prepared by the combined hydrothermal-solvothermal technique. Several ZnO-NR-QD-NAs with different shell thickness (L) were prepared in this experiment by controlling the solvothermal reaction time (t) for growing ZnO-QDs. With the reaction times of t = 4, 4.5, and 6 h, the L = 5, 8, and 16 nm were obtained, respectively (see Figure S2 in the Supporting Information). In comparison to the original ZnO nanorods (Figure 2d), more irregular terminations of lattice periodicity appear inside the shell and on the shell surface (Figure 2f), indicating a higher concentration of defects is introduced into the shell.[38]

With increasing L (i.e., reaction time t), more surface defects are produced in ZnO-NR-QD-NAs, as is characterized by photoluminescence (PL) spectra (Figure 3). The ZnO-NA

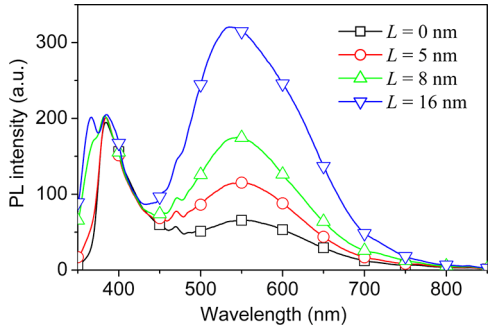

Figure 3. Room temperature PL spectra of original ZnO-NA (L = 0 nm) and ZnO-NR-QD-NAs with L = 5, 8, and 16 nm.

sample exhibits a sharp emission at 382 nm and a broad emission peak at 500−600 nm. The emission at 382 nm is regarded as near band edge (NBE) emission, and the broad emission is attributed to the deep level emission (DLE) due to intraband surface defects,[39] such as oxygen vacancy (V_O), zinc vacancy (V_{Zn}), oxygen interstitial (O_i), zinc interstitial (Zn_i), and oxygen antisites (O_{Zn}).[40] In the ZnO-NR-QD-NAs, the similar NBE emission and DLE peaks are observed, where the NBE emission intensity is almost unchanged but the DLE intensity increases dramatically as L increases, suggesting that the NBE emission is mainly from the ZnO nanord core and the increased DLE is related to the shell formation. The intensity ratio between the DLE and NBE emission is an indication of crystal quality, and a larger ratio means a higher concentration of surface defects.[39] Since the intensity of NBE emission in all the samples is quite similar, the higher DLE intensity in ZnO-NR-QD-NAs with increasing L actually indicates a higher defect concentration. In addition, an emission at 366 nm is observed and its intensity gets increased with increasing L, which has been recognized as the NBE emission of ZnO-QDs with a size less than 5 nm.[41] Hence, the appearance of the NBE peak at 366 nm further confirms the formation of shell consisting of ZnO-QDs in the ZnO-NR-QD-NAs.

3.2. Solar Cells. *3.2.1. Device Performance.* Figure S3 (Supporting Information) shows that MEH-PPV can compactly fill the interspaces between either ZnO-NA or ZnO-NR-QD-NA nanorods after thermal annealing (150 °C, 20 min), which is the same as the observation in our previous results[13,32,34] and the reports on the polymer infiltration in ZnO-TiO_2-NAs[16] or CdS-QDs and CdSe-QDs cosensitized ZnO-NAs[42] by others. To investigate the device photovoltaic performance related to formation of core/shell structure, we compare J−V behaviors of the devices based on the as-synthesized ZnO-NA and ZnO-NR-QD-NAs under simulated AM1.5 illumination (100 mW/cm^2) (Figure 4a). The averaged overall photovoltaic performance of three individual devices for each sample is presented in Table 1. The MEH-PPV/ZnO-NA device exhibits a rather low V_{oc} (<0.4 V), similar to the previous reports on P3HT/ZnO-NA[8,9,43] and MEH-PPV/ZnO-NA.[13] In contrast, the ZnO-QDs shell

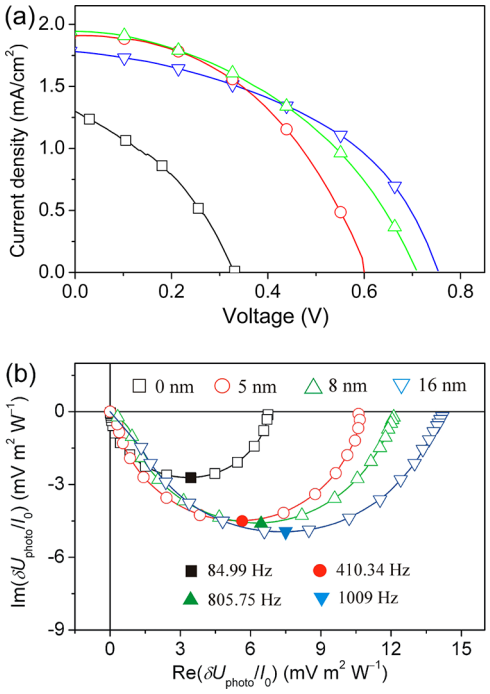

Figure 4. (a) $J-V$ curves under AM1.5 illumination and (b) IMVS spectra of the solar cells based on ZnO-NA (□) and ZnO-NR-QD-NAs with L = 5 nm (○), 8 nm (△), and 16 nm (▽). The solid symbols in b identify the f_{min} points.

formation improves significantly J_{sc} and V_{oc}, depending on L. The device V_{oc} increases rapidly from 0.36 V for L = 0 nm to 0.74 V for L = 8 nm; further increasing L up to ~16 nm only leads to a very slight increase in V_{oc}. However, the device J_{sc} first increases when L increases from 0 to 8 nm, and then decreases for further increasing L, which is similar to the previously observed J_{sc} dependences on the TiO_2 shell thickness in P3HT/ZnO-TiO_2-NA solar cells[15] and the amount of CdS-QDs in CdS-sensitized MEH-PPV/ZnO-NA devices.[18]

Here we first discuss the L-dependence of J_{sc}. Our previous theoretical simulations revealed that the photocurrent in MEH-PPV/ZnO-NAs solar cells originates dominantly from the exciton dissociation at the MEH-PPV/ZnO interfaces formed by the side faces of ZnO nanorods.[32] Because of the short diffusion length of excitons in MEH-PPV (~5−8 nm),[44−46] only the excitons within the exciton diffusion length of the MEH-PPV/ZnO interface lead to free charge carriers. The interspacings between the ZnO nanorods in the as-synthesized ZnO-NA are not uniform and distributed from tens to hundred nanometers (Figure 2a), and mostly in the range of 5−50 nm consistent with Yang's report.[35] Statistically, the interspacing between the ZnO nanorods in the ZnO-NA is averaged to be 25 nm.[35,47] On the basis of the averaged ZnO nanorod interspacing in ZnO-NA and the diffusion length of excitons in MEH-PPV, it is theoretically predicted[47] that an optimized shell thickness (L_{opt}) (regardless of the shell composition) of 4−8 nm exists for the efficient charge generation, and the polymer contribution to J_{sc} will not be influenced for the shell with a thickness of $L \leq L_{opt}$ but be reduced as $L > L_{opt}$. The presence of the peak J_{sc} at L = 8 nm agrees well with our theoretical prediction. Moreover, formation of the coarse shell will inevitably increase the interfacial area for exciton dissociation in comparison to the smooth surface of the original ZnO nanorods. The increased J_{sc} with increasing L for $L \leq 8$ nm is explained by the increased interfacial area for exciton dissociation with the shell formation, when the polymer contribution is not affected. Reasonably, with further increasing L up to the value with $L > L_{opt}$, the device J_{sc} will be a competitive result of increased interfacial area for exciton dissociation and decreased polymer amount infiltrated into nanorod interspaces. The decreased J_{sc} upon increasing L up to 16 nm is attributed to the reduced the amount of MEH-PPV between the nanorods,[16,18,47] which leads to a reduced MEH-PPV contribution to J_{sc} that suppresses the contribution from the increased interfacial area for charge generation.

On the other hand, shell formation increases the fill factor (FF) of the solar cells (Table 1), from 36% for L = 0 nm to 45% for L = 5 nm for example, the increase in FF due to the shell formation is attributed to the balanced mobility between photogenerated electrons and holes[4,48,49] as a result of the reduced mobility difference between the charge carriers (refer to later discussion). Furthermore, the shell thickness has a faint influence on the FF (around 45%) in the MEH-PPV/ZnO-NR-QD-NAs solar cells at the first glance (Table 1), but the detailed inspection shows that the FF indeed reduces with increasing L, even though slightly. The similar L-dependence of FF value was also observed in the P3HT/ZnO-TiO_2-NAs devices,[16] for which the reason was not unclear. The slight decrease in FF upon increasing L in this experiment may be due to the reduced shunt resistance (R_{sh}) in device (Table 1).[50]

IMVS is a powerful dynamic photoelectrochemical method to characterize the electron lifetime τ_e related to interfacial charge recombination.[13,34] IMVS measures the photovoltage (δU_{photo}) response to a small sinusoidal light perturbation superimposed on the background light intensity I_0 under open-circuit condition. The measured IMVS responses are shown in Figure 4b, and the observation that a larger V_{oc} is accompanied by a higher photovoltage agrees with previous results.[13,34] The τ_e value was calculated from the frequency (f_{min}) of the lowest imaginary component of IMVS response according to the relation $\tau_e = (2\pi f_{min})^{-1}$ and collected in Table 1. The τ_e values (0.15−1.75 ms) are comparable to our previous reports.[13,34] Clearly, increase in L reduces τ_e, indicating a higher charge

Table 1. Device Performance of MEH-PPV/ZnO-NA (L = 0 nm) and MEH-PPV/ZnO-NR-QD-NAs (L = 5, 8, and 16 nm) Hybrid Solar Cells under AM1.5 Illumination (100 mW/cm²)[a]

L (nm)	V_{oc} (V)	J_{sc} (mA/cm²)	FF (%)	η (%)	τ_e (ms)	R_s (kΩ)	R_{sh} (kΩ)
0	0.36 ± 0.04	1.37 ± 0.05	35.95 ± 1.17	0.17 ± 0.02	1.75 ± 0.22	1.22 ± 0.03	5.28 ± 0.32
5	0.63 ± 0.05	1.69 ± 0.25	44.92 ± 3.46	0.46 ± 0.08	0.36 ± 0.05	1.33 ± 0.19	62.73 ± 0.16
8	0.74 ± 0.03	1.89 ± 0.11	44.23 ± 1.60	0.62 ± 0.03	0.21 ± 0.03	1.19 ± 0.23	34.31 ± 3.54
16	0.76 ± 0.01	1.80 ± 0.16	43.66 ± 2.38	0.59 ± 0.07	0.15 ± 0.02	1.07 ± 0.05	27.06 ± 0.10

[a]Each of the photovoltaic performance data with standard deviations represents the average of three devices. R_s and R_{sh} link with the slope characteristics at V_{oc} and J_{sc}, respectively.

recombination rate in the sample with a thicker shell. HRTEM and PL results have clearly indicated that a higher concentration of surface defects is introduced as L increases (Figures 2f and 3). The smaller τ_e for the thicker shell is reasonably due to the increased defect concentration in shell, because as more electrons are trapped in surface defects they will not easily escape from the MEH-PPV/ZnO-QDs interface where a substantial number of holes exist, resulting in a faster recombination or smaller τ_e.[13,43] Clearly, the L-dependence of τ_e is opposite to that of V_{oc} (Table 1), which will be discussed in the later section.

As shown in Figure 5, the semilogarithmic plots of the $J-V$ characteristics of solar cells in the dark normally exhibit three

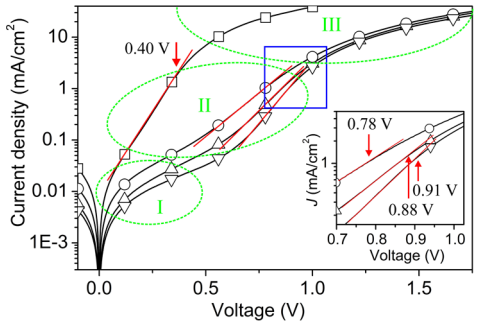

Figure 5. Semilogarithmic plots of $J-V$ characteristic in the dark of the solar cells based on ZnO-NA (□) and ZnO-NR-QD-NAs with L = 5 nm (○), 8 nm (△), and 16 nm (▽). The inset shows the magnified $J-V$ curve in the marked frame, to identify the V_{bi} values in the core/shell samples.

distinct regimes,[28,51] that is, (I) linear increase for leakage-dominated current, (II) exponential increase for diffusion-dominated current, and (III) quadratic increase for space-charge-limited current. The built-in voltage (V_{bi}) corresponding to the built-in electric filed (E_{bi}) due to the work-function (W_f) difference between ITO and Au counter electrodes[34,52] was evaluated at the point where the dark $J-V$ curve begins to follow a quadratic behavior.[28,51] The measured V_{bi} in MEH-PPV/ZnO-NA device is 0.40 V, but much higher V_{bi} is produced with increasing L in MEH-PPV/ZnO-NR-QD-NA devices (Figure 5).

3.2.2. Formation of Dipoles. In MEH-PPV/ZnO-NA solar cells, the charge generation mainly originates from the exciton generated between the nanorods with a length of about 400 nm, in which the excitons mainly dissociate at nanorod side faces.[32] Hence, the behaviors of charge carriers nearby the ZnO nanorod side surface are very important for device performance. After the electron injecting into the ZnO-QDs shell, they will be either injected into the ZnO nanorod core or trapped by the abundant surface defects in the shell, where trapping process will inevitably reduce the electron mobility (μ_e). The μ_e values in MEH-PPV/ZnO-NA and MEH-PPV/ZnO-NR-QD-NA composite films were obtained by space-charge-limited current (SCLC) method,[53−55] using the electron-only devices fabricated by sandwiching the photoactive layers between ITO and LiF/Al electrodes (see Figure S4 in the Supporting Information). The SCLC with field-dependent mobility is given by[55]

$$J_e = \frac{9}{8}\varepsilon_r\varepsilon_0\mu_e\frac{V^2}{L^3}\exp\left(0.891\gamma_e\sqrt{\frac{V}{L_p}}\right) \quad (1)$$

where J_e is the electron current, μ_e the zero-field mobility of electron, γ_e a field activation factor, ε_0 the permittivity of free space, ε_r the relative permittivity of the material, and L_p the thickness of photoactive layer. The $J-V$ characteristics in the dark (J_D-V) of the electron-only devices were fitted to eq 1 to get parameter μ_e (Figure 6). Results show that the shell

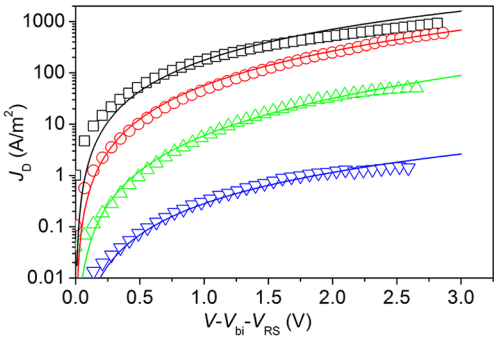

Figure 6. J_D-V of ITO/ZnO:MEH-PPV/LiF/Al electron-only devices with ZnO-NA (□) and ZnO-NR-QD-NAs (○ 5 nm, △ 8 nm, ▽ 16 nm). The solid lines imposed on scatters represent the fits of the experimental data (scatters) using eq 1. The applied voltage (V) corrected for the built-in voltage (V_{bi}) due to the work-function difference between Al and ITO electrodes and the voltage drop (V_{RS}) arising from the resistance of collection electrode. The fits produce the μ_e values of 1.8×10^{-6} (□), 3.9×10^{-7} (○), 3.7×10^{-8} (△), and 2.8×10^{-9} (▽) m^2 V^{-1} s^{-1} in the MEH-PPV/ZnO composite films.

formation leads to the μ_e about 1−3 orders of magnitude lower than that in MEH-PPV/ZnO-NA film, with a smaller μ_e for a larger L. For example, μ_e values are 1.8×10^{-6} and 3.7×10^{-8} m^2 V^{-1} s^{-1} for MEH-PPV/ZnO-NA and MEH-PPV/ZnO-NR-QD-NA with L = 8 nm, respectively. The reduced μ_e upon the shell formation is reasonably resulted from the reduced electron mobility in the shell layer, because the polymer and ZnO nanorod core remain unchanged in the samples.

Clearly, the electrons (e) in the shell and the holes (h) in the polymer in MEH-PPV/ZnO-NR-QD-NA devices have a smaller mobility difference (the hole mobility is 1×10^{-10} m^2 V^{-1} s^{-1} in MEH-PPV[56,57]) than in MEH-PPV/ZnO-NA ones, which will favor the electronic coupling between the electrons and holes to form dipoles directing toward the polymer (negative charge in ZnO-QDs shell and positive charge in polymer), as depicted in Figure 7a; in addition, the dipoles orient along the built-in filed E_{bi} direction toward the counter electrode.[28] Note that, a certain number of dipoles can also be

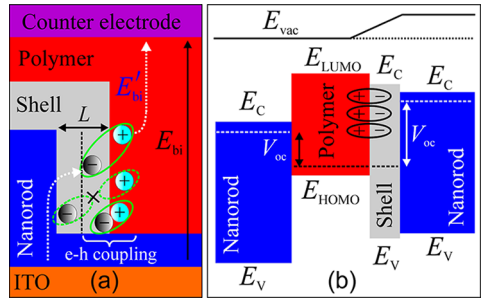

Figure 7. (a) Illustration of interfacial dipole formation, the cross between electron and hole means they are not able to couple with each other. (b) The band structure changes subjected to the core/shell formation, where the dashed lines indicate the quasi-Fermi levels.

produced at the polymer/ZnO interface by the electrons trapped on ZnO nanorods and the hole in the polymer in the MEH-PPV/ZnO-NA system,[58] but formation of core/shell structure eventually increases the dipole number.

Obviously, the photogenerated electrons and holes need to locate within a certain e-h separation where they are spatially close enough to couple with each other (ca. 3−10 nm[59]) for the dipole formation. Therefore, the e-h coupling region for dipole formation is very thin (less than 10 nm) and the dipole formation inevitably correlates with the shell thickness L, resulting in the presence of an expected maximum L of around 10 nm, above which dipole formation will become saturated.[60] As the shell thickness is comparable to the e-h separation for coupling, all the electrons in the shell are capable to form dipoles; however, in the shells with a larger thickness (e.g., L > 10 nm), some injected electrons will diffuse toward the core with a spatial separation beyond the e-h coupling region (Figure 7a) and they will not able to couple with the holes in the polymer to generate dipoles, eventually causing the presence of saturated electron concentration for coupling.

The interfacial dipole shell (directing toward the polymer) can induce an extra polar electric field (E'_{bi}) as an addition to enhance E_{bi} (Figure 7a),[28,61] this is confirmed by the observed L-dependence of V_{bi}. According to the W_f difference between Au (~5.1 eV)[6] and ITO (~4.8 eV),[6] the maximum theoretical V_{bi} in the solar cells is estimated to be about 0.30 V. However, the measured V_{bi} in MEH-PPV/ZnO-NA device is actually 0.40 V, and much higher V_{bi} (0.78−0.91 V) is produced with increasing L in MEH-PPV/ZnO-NR-QD-NA devices (L = 5−16 nm) (Figure 5). All the measured V_{bi} is significantly larger than the theoretical expectation (0.30 V), suggesting the extra voltage contribution to V_{bi} from the dipoles present at the polymer/ZnO interface.[60] The larger V_{bi} in MEH-PPV/ZnO-NR-QD-NA solar cells than in MEH-PPV/ZnO-NA devices demonstrates more dipoles generated due to the shell formation. The L-dependence of V_{bi} indicates a L-dependent dipole formation in the ZnO-QDs shell; in particular, increasing L from 8 to 16 nm leads to a very slight increase in V_{bi} from 0.88 to 0.91 V, indicating the dipole formation has almost become saturated at $L \geq 8$ nm. The observed maximum L of around 8 nm for increasing V_{bi} agrees with the expectation on the dipole formation.

3.2.3. Dipole Effects on V_{oc} and τ_e. Quantum confinement effect will shift the conduction band (E_c) and valence (E_v) edges to increase in band gap of QDs with reducing size. Hence, there exists a band offset between core and shell in ZnO-NR-QD-NAs (Figure 7b), which may increase the energy difference between the HOMO level of the polymer and the E_c edge of the QDs acceptor to affect the V_{oc}.[18,21,62] In this experiment, the increased V_{oc} upon increasing L is reasonably not resulted from the upshift of E_c edge in ZnO-QDs shell due to the quantum confinement effect. On one hand, the E_c shift of ZnO-QDs relative to bulk value is less than 0.13 eV when the particle size is larger than 3 nm (see Figure S5 in the Supporting Information). However, the observed improvement of eV_{oc} in ZnO-NR-QD-NA devices are much larger than the expected maximum from the E_c shift; moreover, a thicker shell inevitably contains larger ZnO-QDs (Figure 2f and Figure S2 in the Supporting Information), the ZnO-NR-QD-NA device with a higher V_{oc} should be observed for thinner shell based on the band-offset standpoint due to a larger energy difference between the polymer HOMO level and the E_c of smaller ZnO-QDs. Therefore, the upshift of the E_c edge in shell due to the quantum confinement effect is not the reason for the increased V_{oc}.

The L-dependences of V_{oc}, V_{bi}, τ_e, and μ_e are depicted in Figure 8. The μ_e values keep a remarkable decrease with

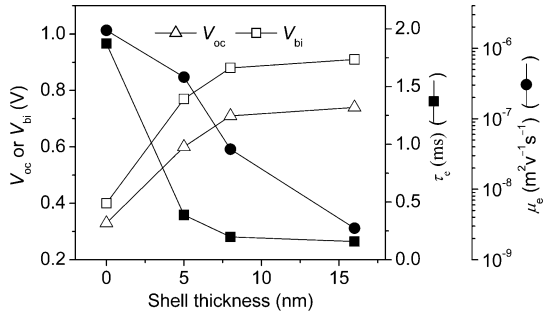

Figure 8. Dependences of V_{oc}, V_{bi}, μ_e, and τ_e on ZnO shell thickness.

increasing L from 0 to 16 nm, for which the increasing surface defect concentration in the growing shell is responsible; however, V_{oc} increases initially when increasing L from 0 to 8 nm and almost remains unchanged with further increasing L up to 16 nm. The different L-dependences of V_{oc} and μ_e infer there is no direct relation between V_{oc} and μ_e, in other words, V_{oc} is not directly determined by μ_e. In contrast, V_{bi} and V_{oc} follow the same changing trend with increasing L, indicating a strong correlation between V_{oc} and dipole formation in the shell.[51,60]

It is believed that the V_{oc} in the MEH-PPV/ZnO-NA and MEH-PPV/ZnO-NR-QD-NA devices is mainly determined by the energy levels of E_c edge in ZnO nanorod core and HOMO band in MEH-PPV, but significantly correlates with the quasi-Fermi levels of the electrons in ZnO nanorod core and the holes in polymer.[13,61,63] With the presence of dipoles directing toward the polymer in shell layer, the E_c of ZnO nanorod core is shifted toward the local vacuum level of the polymer by the interfacial dipole field,[61] along with up-shifting the vacuum level of ZnO nanorod core, while the position of quasi-Fermi level of electrons relative to the E_c of ZnO core is not affected (Figure 7b), as is similar to the interfacial modification with dipole organics in P3HT/TiO_2 and P3HT/ZnO solar cells.[26−28] The E_c of ZnO core is changed by $e\delta E$,[26,61] where δE is the change of surface potential and can be calculated from Poisson's equation, $\delta E = N\mu\cos\theta/\varepsilon_r\varepsilon_0$, where N is the dipole concentration, μ the dipole moment, θ the angle between the dipole and the surface normal, ε_r the dielectric constant of ZnO, and ε_0 the permittivity of free space. Therefore, the magnitude of E_c shifting and thereby the device V_{oc} correlates with the population of dipoles. More dipoles formed by thicker ZnO-QDs shell make a larger energy difference between the quasi-Fermi levels of electrons in ZnO nanorod core and holes in MEH-PPV for a higher V_{oc} in the range of L = 0−8 nm; however, increasing L from 8 up to 16 nm does not cause the remarkable E_c shift in ZnO nanorod core due to the saturated dipole formation and results in the almost unchanged V_{oc}.

The interfacial dipole generation actually can be regarded as formation of a charger-transfer state of weakly bound pairs of electrons and holes within e−h separation of few nanometers by Coulombic attraction,[59,64−67] where the charges may either become free charge carriers after escaping their mutual attraction or recombine to loss energy. The charge recombination may reduce V_{oc}.[68−70] Previous observations on HPSCs[8,27,63,71−77] or dye-sensitized solar cells (DSCs)[78,79] showed that the device with a larger V_{oc} often exhibited a

reduced charge recombination rate (or longer τ_e), which seems to inform that V_{oc} is governed by τ_e in both HPSCs[11,16,18,62] and DSCs.[78,79] Recent results have shown that there is no direct correlation between V_{oc} and τ_e in HPSCs,[13,17,34,47] even though they may change in a similar trend subjected to the same influencing factor.[13,34] The L-dependence of τ_e opposite to that of V_{oc} or V_{bi} further confirms no direct relationship between V_{oc} on τ_e in MEH-PPV/ZnO-NR-QD-NA devices, for which the different effects on V_{oc} and τ_e due to shell formation should be responsible, that is, V_{oc} is dominantly affected by the E_c shift ($e\delta E$) of ZnO core due to dipole field, whereas τ_e is mainly related to the interfacial charge recombination resulting from defect concentration.

3.2.4. Further Evidence from TiO_2 Nanoarrays. To test whether the homogeneous core/shell strategy for improving V_{oc} can be extended to other oxides, solar cells based on TiO_2-NA and TiO_2-NR-QD-NA were examined by the routine depicted in Figure 1. Insets to Figure 9 show the SEM images

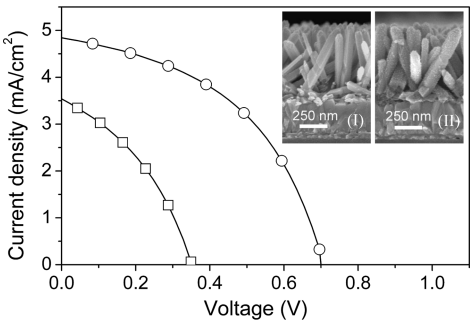

Figure 9. J–V curves of TiO_2-NA (□) and TiO_2-NR-QD-NA (○) solar cells under AM 1.5 illumination. Insets are the SEM images of TiO_2-NA (I) and TiO_2-NR-QD-NA (II).

of TiO_2-NA and TiO_2-NR-QD-NA. Clearly, the TiO_2-NA consists of vertically aligned TiO_2 nanorods with a length of 500 nm and diameter of 40–50 nm (inset I to Figure 9); after TiO_2-QDs deposition, the morphology of TiO_2-NA is not remarkably altered, but the TiO_2 nanorod surfaces are decorated by nanoparticles (inset II to Figure 9). The XRD patterns of the TiO_2-NA samples before and after TiO_2-QDs deposition matched well rutile TiO_2 (see Figure S6 in the Supporting Information). TEM images showed that the original TiO_2 nanorods had quite smooth surfaces, and a core/shell structure was formed after deposition TiO_2-QDs (see Figure S7 in the Supporting Information). HRTEM images (see Figure S7 in the Supporting Information) indicated that the TiO_2 nanorod grew along [001] direction, and the shell consisted of differently oriented TiO_2-QDs of 2–4 nm in size. Therefore, the TiO_2-NR-QD-NA with the single-crystalline TiO_2 nanorod as core and the polycrystalline film (5 nm in thickness) of TiO_2-QDs as shell is successfully by the combined hydrothermal-solvothermal method. Similar to the cases of ZnO nanoarrays, MEH-PPV can also be well infiltrated into the interspaces between either TiO_2-NA or TiO_2-NR-QD-NA nanorods after thermal annealing (150 °C, 20 min) (see Figure S8 in the Supporting Information). The J–V curves of MEH-PPV/TiO_2-NA and MEH-PPV/TiO_2-NR-QD-NA solar cells under AM1.5 illumination are compared in Figure 9. The MEH-PPV/TiO_2-NA device exhibits the V_{oc} of 0.35 V, J_{sc} of 3.54 mA/cm^2, FF of 37.70% and η of 0.47%, whereas the MEH-PPV/TiO_2-NR-QD-NA device shows the V_{oc} of 0.71 V, J_{sc} of 4.85 mA/cm^2, FF of 46.62% and η of 1.60%. The observed V_{oc} of 0.35 V in MEH-PPV/TiO_2-NA device is comparable to reports on P3HT/TiO_2-NA solar cells.[11] The phenomena similar to the cases of ZnO are observed upon the TiO_2-QDs shell formation, including the significant increase in V_{oc} as well as J_{sc}, the greatly reduced μ_e but much higher V_{bi} (μ_e = 9.6 × 10^{-9} $m^2v^{-1}s^{-1}$ and V_{bi} = 0.42 V for MEH-PPV/TiO_2-NA, μ_e = 3.6 × 10^{-11} m^2 V^{-1} s^{-1} and V_{bi} = 0.73 V and for MEH-PPV/TiO_2-NR-QD-NA composites) (see Figure S9 in the Supporting Information). IMVS results (see Figure S10 in the Supporting Information) showed also that the significant reduction in τ_e upon the shell formation from 6.78 to 1.50 ms, confirming no direct relationship between V_{oc} on τ_e in MEH-PPV/TiO_2-NR-QD-NA devices. Note, the observed τ_e in our devices is comparable to the reciprocal of the rate constants for recombination between the electrons in TiO_2 and holes in P3HT determined by transient photovoltage method.[27,77,80] The much larger μ_e in MEH-PPV/ZnO-NA (1.8 × 10^{-6} m^2 V^{-1} s^{-1}) than in MEH-PPV/TiO_2-NA (9.6 × 10^{-9} m^2 V^{-1} s^{-1}) agrees with the fact that electron mobility in ZnO is a least 1–2 order of magnitude higher than in TiO_2.[4,80] Moreover, the FF increases by formation of TiO_2 homogeneous core/shell structure, which is similar to the case of ZnO (Table 1).

4. CONCLUSION

We develop a strategy to significantly increase the V_{oc} in polymer/oxide-nanoarray solar cells by formation of homogeneous core/shell nanoarray, in which single-crystalline nanorod serving as core and the film of corresponding quantum dots acts as shell. The V_{oc} in the hybrid solar cells based on the core/shell nanoarrays is dominantly governed by the quasi-Fermi levels of the electrons in the core and holes in the polymer. The shell formation reduces the mobility difference between the photogenerated electrons in the core and holes in the polymer, creating a dipole layer between the core and the polymer. Upon the dipole layer formation, the E_c edge of core is shifted toward the local vacuum level of the polymer with an increase in the energy difference between the quasi-Fermi levels of the electrons and holes for a higher V_{oc} until the saturated dipole formation at the shell thickness that is comparable to the threshold e–h separation for electronic coupling. Moreover, our results indicate that increasing V_{oc} by the core/shell strategy seems to be not dependent on the kinds of metal oxides.

■ ASSOCIATED CONTENT

Ⓢ Supporting Information

XRD patterns of ZnO-NA and ZnO-NR-QD-NAs; SEM and TEM (HRTEM) images of ZnO-NR-QD-NAs with a time of t = 4 and 6 h; fitting experimental data of ZnO-NA and ZnO-NR-QD-NAs based devices by SCLC method; calculated dependence of ZnO conduction band edge shift ΔE_C on quantum dot size; XRD patterns of TiO_2-NA and TiO_2-NR-QD-NA; TEM and HRTEM images of TiO_2-NA and TiO_2-NR-QD-NA; fitting experimental data of TiO_2-NA and TiO_2-NR-QD-NA based devices by SCLC method; IMVS spectra of solar cells based on TiO_2-NA and TiO_2-NR-QD-NA. This material is available free of charge via the Internet at http://pubs.acs.org.

■ AUTHOR INFORMATION

Corresponding Author

*Tel./Fax: 0086-551-65593171. E-mail: mtwang@ipp.ac.cn.

Author Contributions

F.W. performed the experiments, and drafted the manuscript. Q.C., Z.Q., C.L., and H.Z. participated in the theoretical analysis. W.S. participated in the device preparation. M.W. conceived of the study, and participated in its design and coordination. All authors have read and approved the final manuscript.

Notes

The authors declare no competing financial interest.

■ ACKNOWLEDGMENTS

This work was supported by the "100-Talent Program" of Chinese Academy of Sciences, the Scientific Research Foundation for the Returned Overseas Chinese Scholars, State Education Ministry, the National Natural Science Foundation of China (11274307), the Natural Science Foundation of Anhui Province (1308085ME70), and the President Foundation of Hefei Institute of Physical Sciences.

■ REFERENCES

(1) Xu, T.; Qiao, Q. *Energy Environ. Sci.* **2011**, *4*, 2700−2720.
(2) Huang, J.; Yin, Z.; Zheng, Q. *Energy Environ. Sci.* **2011**, *4*, 3861−3877.
(3) Beek, W. J. E.; Wienk, M. M.; Janssen, R. A. J. *Adv. Funct. Mater.* **2006**, *16*, 1112−1116.
(4) Weickert, J.; Dunbar, R. B.; Hesse, H. C.; Wiedemann, W.; Schmidt-Mende, L. *Adv. Mater.* **2011**, *23*, 1810−1828.
(5) Yu, M.; Long, Y.-Z.; Sun, B.; Fan, Z. *Nanoscale* **2012**, *4*, 2783−2796.
(6) Zhang, Q.; Yodyingyong, S.; Xi, J.; Myers, D.; Cao, G. *Nanoscale* **2012**, *4*, 1436−1445.
(7) Liu, J.; Wang, S.; Bian, Z.; Shan, M.; Huang, C. *Appl. Phys. Lett.* **2009**, *94*, 173107.
(8) Ravirajan, P.; Peiró, A. M.; Nazeeruddin, M. K.; Graetzel, M.; Bradley, D. D. C.; Durrant, J. R.; Nelson, J. *J. Phys. Chem. B* **2006**, *110*, 7635−7639.
(9) Olson, D. C.; Lee, Y. J.; White, M. S.; Kopidakis, N.; Shaheen, S. E.; Ginley, D. S.; Voigt, J. A.; Hsu, J. W. P. *J. Phys. Chem. C* **2008**, *112*, 9544−9547.
(10) Williams, S. S.; Hampton, M. J.; Gowrishankar, V.; Ding, I. K.; Templeton, J. L.; Samulski, E. T.; DeSimone, J. M.; McGehee, M. D. *Chem. Mater.* **2008**, *20*, 5229−5234.
(11) Kuo, C. Y.; Tang, W. C.; Gau, C.; Guo, T. F.; Jeng, D. Z. *Appl. Phys. Lett.* **2008**, *93*, 033307.
(12) Takanezawa, K.; Tajima, K.; Hashimoto, K. *Appl. Phys. Lett.* **2008**, *93*, 063308.
(13) Bi, D.; Wu, F.; Qu, Q.; Yue, W.; Cui, Q.; Shen, W.; Chen, R.; Liu, C.; Qiu, Z.; Wang, M. *J. Phys. Chem. C* **2011**, *115*, 3745−3752.
(14) Thitima, R.; Patcharee, C.; Takashi, S.; Susumu, Y. *Solid-State Electron.* **2009**, *53*, 176−180.
(15) Liao, W.-P.; Hsu, S.-C.; Lin, W.-H.; Wu, J.-J. *J. Phys. Chem. C* **2012**, *116*, 15938−15945.
(16) Greene, L. E.; Law, M.; Yuhas, B. D.; Yang, P. D. *J. Phys. Chem. C* **2007**, *111*, 18451−18456.
(17) Lee, Y. J.; Davis, R. J.; Lloyd, M. T.; Provencio, P. P.; Prasankumar, R. P.; Hsu, J. W. P. *IEEE J. Sel. Top. Quantum Electron.* **2010**, *16*, 1587−1594.
(18) Wang, L.; Zhao, D.; Su, Z.; Li, B.; Zhang, Z.; Shen, D. *J. Electrochem. Soc.* **2011**, *158*, H804−H807.
(19) Hao, Y. Z.; Pei, J.; Wei, Y.; Cao, Y. H.; Jiao, S. H.; Zhu, F.; Li, J. J.; Xu, D. H. *J. Phys. Chem. C* **2010**, *114*, 8622−8625.
(20) Wang, J.; Zhang, T.; Wang, D.; Pan, R.; Wang, Q.; Xia, H. *Chem. Phys. Lett.* **2012**, *541*, 105−109.
(21) Wang, L.; Zhao, D.; Su, Z.; Shen, D. *Nanoscale Res. Lett.* **2012**, *7*, 106.
(22) Fan, X.; Zhang, M.-L.; Shafiq, I.; Zhang, W.-J.; Lee, C.-S.; Lee, S.-T. *Adv. Mater.* **2009**, *21*, 2393−2396.
(23) Wang, K.; Chen, J. J.; Zeng, Z. M.; Tarr, J.; Zhou, W. L.; Zhang, Y.; Yan, Y. F.; Jiang, C. S.; Pern, J.; Mascarenhas, A. *Appl. Phys. Lett.* **2010**, *96*, 123105.
(24) Brabec, C. J.; Cravino, A.; Meissner, D.; Sariciftci, N. S.; Fromherz, T.; Rispens, M. T.; Sanchez, L.; Hummelen, J. C. *Adv. Funct. Mater.* **2001**, *11*, 374−380.
(25) Olson, D. C.; Shaheen, S. E.; White, M. S.; Mitchell, W. J.; van Hest, M. F. A. M.; Collins, R. T.; Ginley, D. S. *Adv. Funct. Mater.* **2007**, *17*, 264−269.
(26) Goh, C.; Scully, S. R.; McGehee, M. D. *J. Appl. Phys.* **2007**, *101*, 114503.
(27) Vaynzof, Y.; Kabra, D.; Zhao, L.; Ho, P. K. H.; Wee, A. T. S.; Friend, R. H. *Appl. Phys. Lett.* **2010**, *97*, 033309.
(28) Ruankham, P.; Macaraig, L.; Sagawa, T.; Nakazumi, H.; Yoshikawa, S. *J. Phys. Chem. C* **2011**, *115*, 23809−23816.
(29) Koster, L. J. A.; van Strien, W. J.; Beek, W. J. E.; Blom, P. W. M. *Adv. Funct. Mater.* **2007**, *17*, 1297−1302.
(30) Mandoc, M. M.; Koster, L. J. A.; Blom, P. W. M. *Appl. Phys. Lett.* **2007**, *90*, 133504.
(31) Shao, S. Y.; Liu, F. M.; Xie, Z. Y.; Wang, L. X. *J. Phys. Chem. C* **2010**, *114*, 9161−9166.
(32) Wu, F.; Shen, W.; Cui, Q.; Bi, D. Q.; Yue, W. J.; Qu, Q. Y.; Wang, M. T. *J. Phys. Chem. C* **2010**, *114*, 20225−20235.
(33) Liu, B.; Aydil, E. S. *J. Am. Chem. Soc.* **2009**, *131*, 3985−3990.
(34) Wu, F.; Yue, W.; Cui, Q.; Liu, C.; Qiu, Z.; Shen, W.; Zhang, H.; Wang, M. *Sol. Energy* **2012**, *86*, 1459−1469.
(35) Greene, L. E.; Law, M.; Tan, D. H.; Montano, M.; Goldberger, J.; Somorjai, G.; Yang, P. D. *Nano Lett.* **2005**, *5*, 1231−1236.
(36) Greene, L. E.; Law, M.; Goldberger, J.; Kim, F.; Johnson, J. C.; Zhang, Y.; Saykally, R. J.; Yang, P. *Angew. Chem., Int. Ed.* **2003**, *42*, 3031−3034.
(37) Wang, Z.-Q.; Ge, R.-P.; Gong, J.-F.; Gu, S.-L.; Yang, S.-G. *Mater. Lett.* **2012**, *82*, 29−32.
(38) Xu, X.; Xu, C.; Lin, Y.; Ding, T.; Fang, S.; Shi, Z.; Xia, W.; Hu, J. *Appl. Phys. Lett.* **2012**, *100*, 172401.
(39) Willander, M.; Nur, O.; Zhao, Q. X.; Yang, L. L.; Lorenz, M.; Cao, B. Q.; Zúñiga Pérez, J.; Czekalla, C.; Zimmermann, G.; Grundmann, M.; Bakin, A.; Behrends, A.; Al-Suleiman, M.; El-Shaer, A.; Che Mofor, A.; Postels, B.; Waag, A.; Boukos, N.; Travlos, A.; Kwack, H. S.; Guinard, J.; Le Si Dang, D. *Nanotechnology* **2009**, *20*, 332001.
(40) Usui, H. *J. Phys. Chem. C* **2007**, *111*, 9060−9065.
(41) Liu, Y.; Morishima, T.; Yatsui, T.; Kawazoe, T.; Ohtsu, M. *Nanotechnology* **2011**, *22*, 215605.
(42) Kim, H.; Jeong, H.; An, T. K.; Park, C. E.; Yong, K. *ACS Appl. Mater. Interfaces* **2013**, *5*, 268−275.
(43) Olson, D. C.; Shaheen, S. E.; Collins, R. T.; Ginley, D. S. *J. Phys. Chem. C* **2007**, *111*, 16670−16678.
(44) Markov, D. E.; Tanase, C.; Blom, P. W. M.; Wildeman, J. *Phys. Rev. B* **2005**, *72*, 045217.
(45) Lewis, A. J.; Ruseckas, A.; Gaudin, O. P. M.; Webster, G. R.; Burn, P. L.; Samuel, I. D. W. *Org. Electron.* **2006**, *7*, 452−456.
(46) Hwang, I.; Scholes, G. D. *Chem. Mater.* **2011**, *23*, 610−620.
(47) Cui, Q.; Liu, C.; Wu, F.; Yue, W.; Qiu, Z.; Zhang, H.; Gao, F.; Shen, W.; Wang, M. *J. Phys. Chem. C* **2013**, *117*, 5626−5637.
(48) Tress, W.; Petrich, A.; Hummert, M.; Hein, M.; Leo, K.; Riede, M. *Appl. Phys. Lett.* **2011**, *98*, 063301.
(49) Mihailetchi, V. D.; Xie, H. X.; de Boer, B.; Koster, L. J. A.; Blom, P. W. M. *Adv. Funct. Mater.* **2006**, *16*, 699−708.
(50) Kim, M.-S.; Kim, B.-G.; Kim, J. *ACS Appl. Mater. Interfaces* **2009**, *1*, 1264−1269.
(51) Mihailetchi, V. D.; Blom, P. W. M.; Hummelen, J. C.; Rispens, M. T. *J. Appl. Phys.* **2003**, *94*, 6849−6854.
(52) Mingebach, M.; Deibel, C.; Dyakonov, V. *Phys. Rev. B* **2011**, *84*, 153201.
(53) Melzer, C.; Koop, E. J.; Mihailetchi, V. D.; Blom, P. W. M. *Adv. Funct. Mater.* **2004**, *14*, 865−970.

(54) Mihailetchi, V. D.; van Duren, J. K. J.; Blom, P. W. M.; Hummelen, J. C.; Janssen, R. A. J.; Kroon, J. M.; Rispens, M. T.; Verhees, W. J. H.; Wienk, M. M. *Adv. Funct. Mater.* **2003**, *13*, 43−46.
(55) Koster, L. J. A.; van Strien, W. J.; Beek, W. J. E.; Blom, P. W. M. *Adv. Funct. Mater.* **2007**, *7*, 1297−1302.
(56) Shi, Q.; Hou, Y.; Lu, J.; Jin, H.; Li, Y.; Li, Y.; Sun, X.; Liu, J. *Chem. Phys. Lett.* **2006**, *425*, 353−355.
(57) Li, M. H.; Chen, H.-L.; Huang, Y.-F.; Chuang, W.-T.; Chen, Y.-R.; Tsai, H.-S.; Semenikhin, O. A.; White, J. D. *Chem. Phys. Lett.* **2011**, *505*, 100−105.
(58) Ramsdale, C. M.; Barker, J. A.; Arias, A. C.; MacKenzie, J. D.; Friend, R. H.; Greenham, N. C. *J. Appl. Phys.* **2002**, *92*, 4266−4270.
(59) Moliton, A.; Nunzi, J.-M. *Polym. Int* **2006**, *55*, 583−600.
(60) Ramsdale, C. M.; Arias, A. C.; MacKenzie, J. D.; Friend, R. H.; Greenham, N. C. *Mater. Res. Soc. Symp. Proc.* **2002**, *725*, 179−190.
(61) Krüger, J.; Bach, U.; Grätzel, M. *Adv. Mater.* **2000**, *12*, 447−451.
(62) Spoerke, E. D.; Lloyd, M. T.; McCready, E. M.; Olson, D. C.; Lee, Y.-J.; Hsu, J. W. P. *Appl. Phys. Lett.* **2009**, *95*, 213506.
(63) Lin, Y. Y.; Chu, T. H.; Li, S. S.; Chuang, C. H.; Chang, C. H.; Su, W. F.; Chang, C. P.; Chu, M. W.; Chen, C. W. *J. Am. Chem. Soc.* **2009**, *131*, 3644−3649.
(64) Kawatsu, T.; Coropceanu, V.; Ye, A. J.; Brédas, J. L. *J. Phys. Chem. C* **2008**, *112*, 3429−3433.
(65) Zhu, X. Y.; Yang, Q.; Muntwiler, M. *Acc. Chem. Res.* **2009**, *42*, 1779−1787.
(66) Kippelen, B.; Brédas, J.-L. *Energy Environ. Sci* **2009**, *2*, 251−261.
(67) Marsh, R. A.; McNeill, C. R.; Abrusci, A.; Campbell, A. R.; Friend, R. H. *Nano Lett.* **2008**, *8*, 1393−1398.
(68) Potscavage, W. J., Jr.; Yoo, S.; Kippelen, B. *Appl. Phys. Lett.* **2008**, *93*, 193308.
(69) Potscavage, W. J., Jr.; Sharma, A.; Kippelen, B. *Acc. Chem. Res.* **2009**, *42*, 1758−1767.
(70) Vandewal, K.; Tvingstedt, K.; Gadisa, A.; Inganäs, O.; Manca, J. V. *Phys. Rev. B* **2010**, *81*, 125204.
(71) Lin, Y.-Y.; Chu, T.-H.; Chen, C.-W.; Su, W.-F. *Appl. Phys. Lett.* **2008**, *92*, 053312.
(72) Kudo, N.; Honda, S.; Shimazaki, Y.; Ohkita, H.; Ito, S.; Benten, H. *Appl. Phys. Lett.* **2007**, *90*, 183513.
(73) Jiang, K.-J.; Manseki, K.; Yu, Y.-H.; Masaki, N.; Suzuki, K.; Song, Y.-L.; Yanagida, S. *Adv. Funct. Mater.* **2009**, *19*, 2481−2485.
(74) Said, A. J.; Poize, G.; Martini, C.; Ferry, D.; Marine, W.; Giorgio, S.; Fages, F.; Hocq, J.; Bouclé, J.; Nelson, J.; Durrant, J. R.; Ackermann, J. *J. Phys. Chem. C* **2010**, *114*, 11273−11278.
(75) Peiró, A. M.; Ravirajan, P.; Govender, K.; Boyle, D. S.; O'Brien, P.; Bradley, D. D. C.; Nelson, J.; Durrant, J. R. *J. Mater. Chem.* **2006**, *16*, 2088−2096.
(76) Bouclé, J.; Chyla, S.; Shaffer, M. S. P.; Durrant, J. R.; Bradley, D. D. C.; Nelson, J. *Adv. Funct. Mater.* **2008**, *18*, 622−633.
(77) Tai, Q.; Zhao, X.; Yan, F. *J. Mater. Chem.* **2010**, *20*, 7366−7371.
(78) Hara, K.; Miyamoto, K.; Abe, Y.; Yanagida, M. *J. Phys. Chem. B* **2005**, *109*, 23776−23778.
(79) Snaith, H. J.; Moule, A. J.; Klein, C.; Meerholz, K.; Friend, R. H.; Grätzel, M. *Nano Lett.* **2007**, *7*, 3372−3376.
(80) Quintana, M.; Edvinsson, T.; Hagfeldt, A.; Boschloo, G.. *J. Phys. Chem. C* **2007**, *111*, 1035−1041.